analytical chemistry

pubs.acs.org/ac Article

Tandem Raman and Elemental Aerosol Spectrometer (TREAS) for Near-Real-Time Aerosol Chemical Speciation

Pramod Kulkarni,* Nicholas Pugh, Orthodoxia Zervaki, Kabir Rishi, and Surendra Devarakonda

Cite This: *Anal. Chem.* 2026, 98, 11923−11934 Read Online

ACCESS | Metrics & More | Article Recommendations | Supporting Information

ABSTRACT: Current methods for quantifying aerosol chemical exposures rely primarily on filter-based collection and off-line laboratory analysis, resulting in significant delays in chemical risk assessment. We describe the development and evaluation of the Tandem Raman and Elemental Aerosol Spectrometer (TREAS), a compact instrument designed for the near-real-time measurement of trace elemental and molecular speciation in workplace atmospheres. TREAS employs an automated, cyclical "collection-analysis-ablation" scheme, in which aerosols are focused onto a dry spot, analyzed by Raman spectroscopy (RS), and subsequently ablated by pulsed spark discharges for elemental quantification via spark emission spectroscopy (SES). Laboratory evaluation using occupationally relevant aerosols in the $PM_{2.5}$ size fraction, specifically crystalline silica (α-quartz) and titanium dioxide (TiO_2), demonstrated mass limits of detection (LOD) that were significantly lower than those of standardized X-ray diffraction and infrared methods. The LODs for α-quartz were 420 ng (RS) and 900 ng (SES), while LODs for TiO_2 were 155 ng (RS) and 250 ng (SES). Beyond quantification, the tandem approach provided complementary chemical insights: while SES quantified trace elements, RS can successfully distinguish between the chromium(VI) and chromium(III) oxidation states in welding fumes. The study demonstrates the potential of TREAS to provide high-sensitivity, automated, and analyte-specific monitoring of complex aerosol exposures in near real-time.

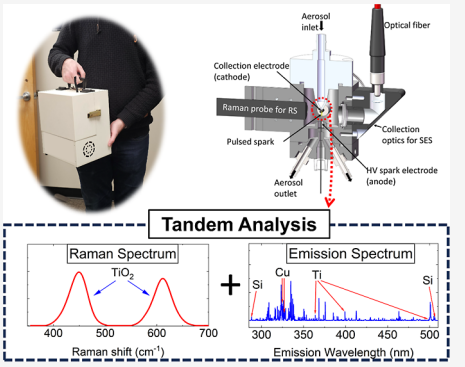

INTRODUCTION

Exposure to hazardous aerosols in ambient and workplace environments can pose significant risks to human health.[1,2] The established methods for quantifying aerosol chemical components, particularly for exposure measurements, rely primarily on filter-based collection and subsequent laboratory analysis with various analytical instruments, resulting in lengthy turnaround times.[3,4] There is a continuing need to develop field-portable, compact instruments and sensors that enable analyte-specific quantitative measurements to advance exposure science research.[5,6] On-site rapid analysis is also essential for immediate hazard identification and mitigation, as well as for emergency response.

Significant progress has been made in real-time chemical speciation of aerosol particles.[7,8] Single-particle analysis techniques, such as mass spectrometric detection methods, including Aerosol Mass Spectrometers, provide detailed information on the chemical components and speciation of aerosols.[9,10] These measurement tools are indispensable for atmospheric chemistry studies. More recently, other near real-time spectroscopic methods have been developed, such as the X-ray fluorescence methods[11] and the infrared absorption methods.[12] However, these are impractical tools (due to their size, weight, and cost) for field-portable, hand-held, or routine aerosol-exposure measurement applications, particularly in indoor air or occupational environments. To address these needs, our laboratory has been investigating several micro-plasma-based atomic-emission techniques suitable for compact, hand-portable instrumentation for portable field exposure measurement. These include aerosol analysis using laser-induced breakdown spectroscopy,[13] corona-assisted microwave-induced plasma spectroscopy,[14] glow-discharge spectroscopy,[15] and spark emission spectroscopy.[16−18] We have shown that adequate detection limits for exposure measurements can be achieved for all relevant particulate metals using a coaxial electrode system that employs dc corona-based aerosol collection, followed by ablation with a pulsed spark discharge.[16−18] The compact, hand-held instrument was developed and deployed in several field studies. The ability to simultaneously measure over 25 elements, including carbon, at a time resolution of a few seconds to a few minutes and detection limits of 0.01 to 1 $\mu g/m^3$ was demonstrated.[19] Its performance was evaluated across different indoor and workplace settings, and the measurements were compared with time-integrated filter measurements to demonstrate the

Received: January 2, 2026
Revised: April 1, 2026
Accepted: April 7, 2026
Published: April 15, 2026

https://doi.org/10.1021/acs.analchem.5c08252
Anal. Chem. 2026, 98, 11923−11934

applicability of the spark-emission-based technique for particulate-metal measurement.[18]

Our work demonstrated that the pulsed spark microplasma-based technique is particularly suited for developing low-cost, compact, and robust field instrumentation for aerosol elemental analysis. The application of this technique has recently been extended to atmospheric particulate matter analysis[20] and occupational measurement[21] applications.

Several recent studies have employed benchtop or research-grade Raman systems for quantitative molecular speciation of aerosols. Raman spectroscopy, while promising,[22−24] faces challenges due to weak scattering, poor sampling statistics, sample fluorescence background (for complex organic samples), and the need for relatively high-power lasers and precision optics, making it impractical for field-portable use. Some recent portable Raman instruments that collect particles on filter tape require manual tape replacement, remain bulky, and have not been fully evaluated, limiting their suitability for exposure monitoring.[25,26] Our recent work has shown that by concentrating the particulate sample over a small spot, adequate detection limits for various analytes can be obtained using commercial field-portable Raman spectrometers.[27−29]

In this study, we describe the design of a compact, hand-portable Tandem Raman and Elemental Aerosol Spectrometer (TREAS) instrument that enables aerosol measurement with high specificity and sensitivity for mixed aerosol exposures in near real-time, addressing many of the drawbacks of the traditional techniques discussed above. The instrument uses two orthogonal spectroscopy techniques in tandem to obtain atomic and molecular characterization of aerosols. In TREAS, an automated cyclical scheme involving collection-analysis-ablation is adopted to obtain continuous measurements using Raman and Spark Emission Spectroscopy. Raman spectroscopy (RS) can selectively identify specific vibrational modes of organic and inorganic substances in chemical, biological, and particulate aerosols,[25,30,31] while spark emission spectroscopy (SES) can be used for elemental identification and quantitation.[16−18]

TREAS showed low LODs for hazardous workplace aerosols (α-quartz and titanium dioxide) using both RS and SES techniques. This was achieved through spot sampling at modest flow rates and collection times (from a few seconds to a few minutes for most analytes). Elemental quantification in TREAS allows application to broad exposure problems. In contrast, molecular characterization through RS allows high-specificity measurement involving polymorphs (e.g., SWCNT v/s graphene), crystallinity (amorphous v/s crystalline silica), and specific oxidation states (e.g., distinguish Cr (VI) from Cr (III)). The automated near-real-time capability of the field-portable TREAS was evaluated by continuously measuring titanium dioxide aerosol. The instrument design, calibration process, analytical figures of merit, and quantification and characterization of field aerosols are presented. We demonstrate that the tandem technique enables the application of TREAS to broad aerosol assessment applications involving complex chemical mixtures, speciation, and oxidation states.

Tandem Raman and Elemental Aerosol Spectrometer

TREAS involves two hyphenated spectroscopic techniques to provide elemental and molecular composition of airborne particles and builds on previous methods developed for aerosol analysis using spark emission spectroscopy[15−18,30] and Raman spectroscopy.[28] A "collection-analysis-ablation" scheme is employed to obtain continuous automated measurements. Airborne particles are first sampled from the air and collected as a dry spot on a rotating electrode; the dry spot is then analyzed by Raman spectroscopy (RS), followed by elemental analysis using pulsed spark emission spectroscopy (SES).

Instrument Design

The overall layout of the different components of TREAS is shown in Figure S1 in the Supporting Information. The instrument consists of three main sections: (a) an aerosol collection system (ACS), (b) a laser Raman spectrometer, and (c) a pulsed spark generator and optical emission spectrometer. The components in the system, powered by an onboard supply, are electronically controlled using an embedded microcontroller. The data acquisition system (LabVIEW, National Instruments) allows for automated measurements. Aerosols are sampled through a converging nozzle onto an electrode in the ACS. The collected particulates are excited using a laser source, and the characteristic Raman vibration modes are detected through the probe. The Raman signal is recorded by the spectrometer, following which the collected particles are ablated using a high-voltage spark generator and measured using the optical emission spectrometers. The field-portable TREAS instrument prototype measures 28 × 28 × 19 cm (H×W×D) and was fabricated using commercially available optical spectrometers. The prototype instrument is shown in Figure S1 in the Supporting Information.

The overall measurement scheme comprises the following cyclical procedures: (i) the collection of aerosol particles on the electrode within the ACS for a specified duration, (ii) a 90° counterclockwise rotation of the electrode, (iii) the acquisition of Raman spectra at predetermined signal integration times followed by spectral analysis for quantification of aerosol mass, (iv) an additional 90° counterclockwise rotation of the electrode (i.e., 180° rotation with respect to initial orientation in step (i) above), (v) the removal of the sample via ablation accompanied by the simultaneous acquisition of emission spectra, and (vi) the return to the initial position, as described in the next section.

Aerosol Collection System (ACS)

The aerosol collection method relies on impaction-based collection. A cross-sectional view of the ACS used in the instrument is shown in Figure 1a. Airborne particles are collected using a size-selective inlet. A $PM_{2.5}$ inlet was used in this study to ensure compatibility with other reference instruments, such as QCM impactors; however, respirable or thoracic inlets can also be used depending on the application. Subsequently, size-selected aerosol particles are focused onto a tungsten collection electrode through a converging nozzle with an orifice diameter of 0.5 mm for a predetermined time. The collection electrode offers a narrow planar surface, facing the nozzle orifice, to facilitate particulate deposition through impaction, as shown in the inset in Figure 1a. At a flow rate of 0.5 L min^{-1}, the collection efficiency of the nozzle, obtained via finite-element simulation of flow and particle transport (COMSOL), reduced below 50% for particles smaller than 0.75 μm (Figure S2 in the Supporting Information).

The single-stage nozzle used in this study was modified from the one used in a previous study[32] to obtain a smaller spot sample in TREAS. Experimental and theoretical (obtained using fluid-dynamic simulations) collection efficiency curves in Zervaki et al.[32] were in reasonable agreement for both a single-stage converging nozzle and a much more complex multistage

https://doi.org/10.1021/acs.analchem.5c08252
Anal. Chem. 2026, 98, 11923−11934

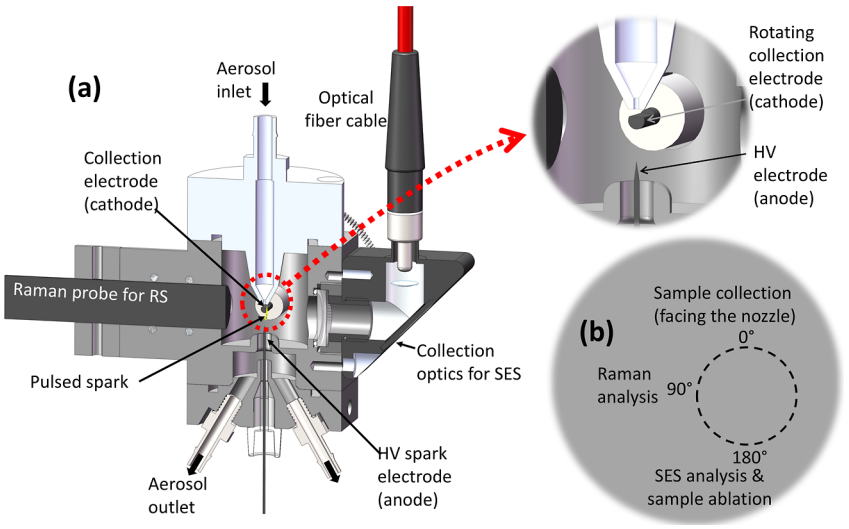

Figure 1. (a) A cross-sectional view of the Aerosol Collection System (ACS) within TREAS is shown. Airborne particles are sampled onto the collection electrode through a converging nozzle. The collected particles are first analyzed with the Raman probe, followed by atomic emission analysis during pulsed spark discharge. An inset at the top right shows a magnified view of the nozzle exit and electrode region. The rotating collection electrode acts as the cathode, while the bottom coaxial electrode serves as the anode during spark discharge (b) Rotational sequence of electrode orientations in TREAS used for particle collection, Raman analysis, spark ablation, and atomic emission analysis.

nozzle. We did not experimentally measure the collection efficiency of the modified nozzle used in TREAS; however, we assumed that the modeled collection efficiency (shown in Figure S2 in Supporting Information) is a good approximation.

The rotating electrode (1.5 mm diameter and 56 mm long; Knd3981, ESPI Metals, Ashland, OR) is driven by a geared stepper motor (model 42M048C2B-R21, Portescap, West Chester, PA) with a rotational step size of 0.75°, serving as the cathode for spark discharge generation. The aerosol flow through the ACS is driven by a miniature pump (Premotec BL30 EB, Allied Motion, Amherst, NY) that is maintained at a specified flow rate using a proportional-integral-derivative (PID) controller with feedback from a flowmeter.

Raman Measurement

Following a 90° rotation of the collection electrode, the particulate sample deposited on the electrode is subjected to analysis via Raman spectroscopy, as shown in Figure 1b, utilizing an integrated Raman probe that provides the excitation source and collects the Raman signal, a laser source, and a spectrometer (Model WP 785, Wasatch Photonics, Morrisville, NC). The Raman probe is incorporated with the ACS, with the excitation laser incident perpendicularly to the planar collection surface of the electrode. The distance between the probe and the collection surface is maintained at 22 mm. The excitation wavelength employed is 785 nm, with a maximum output power of 450 mW and a focal spot diameter of 120 μm. The spectrometer records the intensity over Raman shifts from 235 to 2000 cm^{-1} at a spectral resolution of 6 cm^{-1}. A 3 s integration time was used to optimize the signal-to-noise ratio for the materials analyzed. Raman spectra were acquired at the maximum laser power.

Elemental Measurement

Once the Raman analysis is completed, the collection electrode is rotated a further 90° (180° from the initial orientation used for aerosol collection; Figure 1b) to face the high-voltage electrode (a sharp tungsten electrode; Knd3981, ESPI Metals, Ashland, OR) with a tip diameter of approximately 10 μm. The particulate sample (deposited on the collection electrode) is ablated using a sequence of pulsed spark discharges between the collection electrode (cathode) and the tungsten electrode (anode), using the high-voltage pulse generator (Firefly, Cascodium Inc., Andover, MA) with an output energy of 200 mJ/pulse and a frequency of 1 Hz. The atomic emission signals from the ablated particles were collected through two optical fiber cables (FCRL-7UV100−0.45-SR, Avantes Inc., Lafayette, CO) placed orthogonally coplanar to the Raman probe. These fibers are connected to two spectrometers (AvaSpec-Mini2048CL, Grating: MN18000−0.25, from 290−450 nm/Grating: MN18000−0.5, from 450−590 nm, Avantes Inc., Lafayette, CO). A delay time of 5 μs and a gate width of 1000 μs were used.

A total of 60 spark pulses were employed to acquire the cumulative atomic emission signal from each ablation event. An additional 40 spark ablations were introduced to clean the electrode and prepare it for subsequent sample collection cycles. For each collection shot, the instrument records a single emission spectrum by integrating the outputs of two spectrometers covering the entire wavelength range. The resultant spectrum is subsequently baseline-corrected utilizing the Savitzky−Golay Coupled Advanced Rolling Circle Filter (RCF) algorithm.

MATERIALS & METHODS

Instrument Calibration

Aerosols comprising α-quartz (Min-U-Sil 5, US Silica Company, Berkeley Springs, WV) and titanium dioxide (Ti-Pure, C35R4, DuPont Chemicals, Wilmington, DE) were generated for instrument calibration purposes utilizing a fluidized bed aerosol generator (model 3400A, TSI, Inc., Shoreview, MN), as shown schematically in Figure S3 in the Supporting Information. The fluidized bed was operated at an air flow rate ranging from 10 to 12 L min^{-1}, with 3.5 L min^{-1} directed toward a $PM_{2.5}$ personal sampling cyclone (BG14L/BGI4CP, Mesa Laboratories Inc., Lakeview, CO), while the excess airflow was exhausted through a HEPA filter. The outlet of the $PM_{2.5}$ cyclone was connected to a quartz crystal microbalance micro-orifice uniform deposition impactor (QCM MOUDI impactor model 140, TSI Inc., Shoreview, MN) and the TREAS. TREAS was operated at 0.5 L

https://doi.org/10.1021/acs.analchem.5c08252
Anal. Chem. 2026, 98, 11923−11934

min^{-1}, whereas the QCM MOUDI drew 3 L min^{-1}. To account for the total operational flow rate of 10 L min^{-1} for the QCM impactor, additional HEPA-filtered air was supplied at 7 L min^{-1} using a mass flow controller. The QCM impactor measures the mass of aerosols with aerodynamic diameters between 0.045 and 2.44 μm ($PM_{2.5}$) in real time. The aerosol mass collected on the electrode was calculated from the total mass accumulated and recorded by the QCM over a specified period prior to Raman and emission spectral data acquisition.

Raman spectra used to construct the calibration curve were averaged from five measurements per aerosol sample collection cycle. A 5-point Fast Fourier Transform (FFT) algorithm was employed to smooth the instrument's average raw data. Each smoothed spectrum was corrected for baseline using the anchor point obtained via the second-derivative method and connected through spline interpolation.

The Raman spectrum acquired from the background- specifically, the bare tungsten electrode- showed peaks at 449, 495, and 608 cm^{-1}, which interfered with the α-quartz and TiO_2 peaks of interest at 465 and 610 cm^{-1}, respectively. Peak deconvolution was applied within the Raman shift range of 356−550 cm^{-1} to isolate the α-quartz at 465 cm^{-1}. However, deconvolution was not effective for the TiO_2 peak at 610 cm^{-1}, since it lies too close to the background peak at 608 cm^{-1}. Therefore, the background peak was subtracted from the spectra of the TiO_2 calibration samples, to isolate the corresponding Raman intensity. The baseline-corrected peak height at the Raman shift of interest was utilized to generate the calibration curves for TiO_2 and α-quartz.

The peak height from the spark emission spectra, determined as the difference between the instrument response and the average background intensity at the wavelength of interest for a specific element, was employed to construct the calibration curves.

Field and Laboratory Test Aerosol

Performance of TREAS was investigated using representative workplace aerosol samples. Instrument's measurement sensitivity was probed using aerosolized samples of α-quartz-containing dust (obtained during stone grinding operations) and TiO_2. The instrument's specificity for other analytes was also examined using aliquots of colloidal suspensions deposited directly on the collection electrode of TREAS as described below.

Crystalline Silica-Containing Workplace Aerosols

Aerosols from commercial engineered stone products (A and B) were generated in the wind-tunnel test chamber by manual grinding using a hand-held pneumatic angle grinder (GPW-216, Gison Machinery Co., Ltd., Taiwan) equipped with a medium grit segment cup wheel (Model S-04HDZGX3-M, 4-in. Dia., turbo rim, Diamond Vantage, Irvine, CA). These aerosols have been shown to contain crystalline silica, posing significant health risks.[33] The operation of the test chamber and the test protocol for generating aerosols from engineered stone are described in detail elsewhere.[34] Briefly, this wind-tunnel-like laboratory testing system was designed (in accordance with European Standard EN 1093-3) and housed an automated testing chamber that simulated the emission of aerosol particles generated during the grinding of materials. The airflow through the automated testing chamber was approximately 0.17 m^3/s and was monitored using a calibrated Delta tube and micromanometer. Isokinetic sampling ports ensured representative size-selective sampling and measurements. Incoming air was filtered through prefilters and HEPA filters to remove background particles and maintain uniform airflow.

The aerosol generated from the grinding of engineered stone A (in the wind tunnel chamber) was directly sampled into the TREAS inlet. Aerosol from engineered stone B could not be directly sampled in real-time by TREAS due to logistical constraints. Instead, the settled dust on the chamber floor from grinding the engineered stone B was collected and subsequently aerosolized in the laboratory using the vortex-shaking method[35] to obtain the test aerosol.

A sample of fracking sand dust (FSD) collected at an oil and gas extraction site[28,36] was utilized as a representative occupational aerosol. The physicochemical and biological properties of FSD have been documented in previous studies.[36,37] FSD was aerosolized employing the vortex-shaking method[35] to prepare the test sample. All aerosols were collected for 2 min (i.e., sampling time), followed by spectral analysis using TREAS.

Carbonaceous Aerosols

Carbon-based materials such as multiwalled carbon nanotubes or MWCNTs (OH Functionalized, Outer diameter 10−30 nm, US Research Nanomaterials, Inc., Houston, TX),[30] Diesel Particulate Matter or DPM (NIST SRM 2975; U.S. Department of Commerce, NIST, Gaithersburg, MD), and carbon black (REGAL 400R, Cabot Corporation, Billerica, MA)[17] were suspended in ultrafiltered DI water and directly pipetted onto the TREAS electrode. Spectra were acquired once the sample dried.

Welding Aerosols

An aqueous solution containing hexavalent chromium (NIST SRM 2109; U.S. Department of Commerce, NIST, Gaithersburg, MD) and an aqueous suspension of trivalent chromium oxide powder (393703-100G, Sigma-Aldrich, Saint-Louis, MO) were directly pipetted onto the TREAS collection electrode. The hexavalent chromium was used to obtain a spark emission spectrum, while the trivalent chromium oxide powder was used to obtain both Raman and spark emission spectrum. All spectra were acquired after the deposited aliquots had dried at room temperature. A stainless steel welding fume reference material (HSE SSWF-1; Health and Safety Executive, United Kingdom) was used to assess TREAS's ability to speciate metals in welding aerosol, using both RS and SES. The aerosolized welding fume sample was generated using a medical nebulizer (Salter 8900 Series; Salter Laboratories, Arvin CA), containing a 1 g L^{-1} suspension of the welding fume material and operated at a flow rate of 4−5 L min^{-1}. The droplet stream was dried through a sequence of diffusion dryers, and the dried particles were sampled by TREAS, deposited onto the collection electrode, and subsequently analyzed. Finally, the Raman spectra of chromite ($FeCr_2O4$) sourced from California, USA, and crocoite ($Pb(CrO_4)$) sourced from Dundas, Tasmania, were obtained from the literature, with an excitation wavelength of 780 and 785 nm, respectively (ID R110060 and ID R040053).[38]

RESULTS AND DISCUSSION

Calibration Curves for Titanium Dioxide and α-quartz Aerosols

The calibration curves for TiO_2 are shown in Figure S4 in the Supporting Information. The Raman (red symbols) signal (using peak height at 610 cm^{-1}) and the atomic emission (blue symbols) signal (using the 498.2 nm line) as a function of titanium dioxide (closed circles) mass collected on the TREAS collection electrode are used to construct two calibration curves (corresponding to RS and SES). The Raman mode at approximately 610 cm^{-1} corresponds to the antisymmetric bending vibration of O−Ti−O,[39−41] while the emission line at 498.2 nm is associated with the $3d^3(4F)4p$ to $3d^3(4F)4s$ transition.[42]

We note that the mass of analyte calculated to construct the calibration curve in this study is the gravimetric mass of the analyte derived from its air concentration measured at the inlet using a real-time QCM impactor, the sampling flow rate, and the duration of sample collection by TREAS. Additionally, it is assumed that the impaction collection efficiency is 100%, an assumption that may not be valid depending on the aerosol size distribution being sampled. Notably, the collection efficiency of the nozzle-electrode system decreases significantly for particles with diameters less than 0.75 μm (Figure S2 in the Supporting Information). Assuming complete collection could therefore introduce substantial calibration errors, especially if

https://doi.org/10.1021/acs.analchem.5c08252
Anal. Chem. 2026, 98, 11923−11934

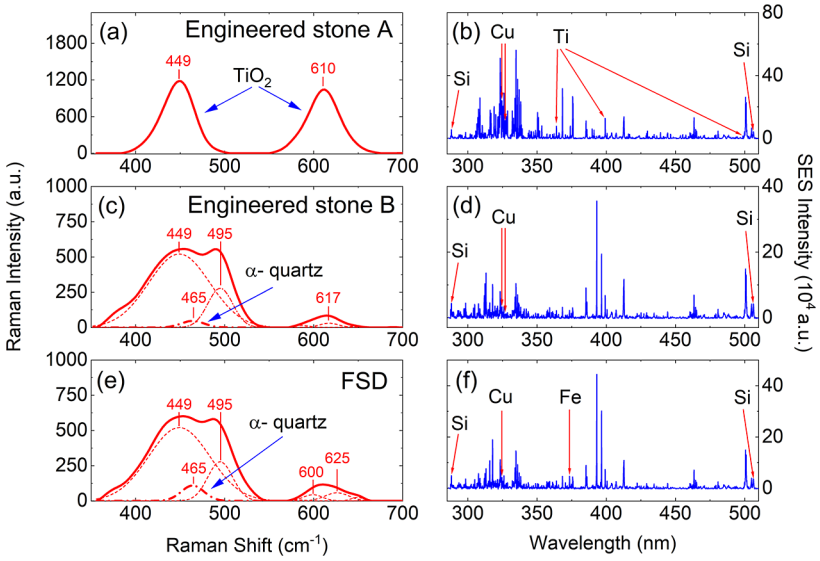

Figure 2. (a) Raman (left) and (b) emission (right) spectra of aerosols from engineered stone A, (c) Raman and (d) emission spectra for engineered stone B, and (e) Raman and (f) emission spectra for FSD, measured using TREAS. Raman spectrum of engineered stone A in (a) is corrected using the background spectrum.

the aerosol contains a significant proportion of fine or ultrafine particles smaller than 0.75 μm in diameter. The calibration aerosols employed in this study have a much larger geometric mean diameter, with only a minor fraction of mass below 0.75 μm, which will likely minimize this error.[43−45] As discussed later, we acknowledge that the size-dependent collection efficiency of the impaction-based collection used in TREAS is a limitation. These limitations are being addressed by incorporating a more efficient, high-throughput aerosol collection method.[46,47]

The calibration curves for crystalline silica are also shown in Figure S4 in the Supporting Information. The Raman signal (using peak height at 465 cm^{-1}) and the emission signal (using the 288.2 nm line) were plotted as a function of the α-quartz (open circles) mass deposited on the collection electrode of TREAS. The Raman mode observed at approximately 465 cm^{-1} is associated with the symmetric stretching-bending of Si−O−Si,[27,48] while the emission line at 288.2 nm corresponds to the $3s^2$ 3p4s to $3s^23p^2$ transition.[42]

The calibration curve was generated by depositing varying quantities of particulate mass from the aerosol containing the analyte. Deposited mass was varied by changing the sample collection time at a fixed aerosol concentration and flow rate. An alternative method would be to vary the inlet aerosol concentration and calibrate the spectroscopic signal directly to the analyte's known inlet air concentration. However, varying analyte air concentrations over 2 orders of magnitude posed several experimental challenges and could not be used in this study. The fluidized-bed technique used to aerosolize the reference materials required maintaining a relatively narrow range of sample flow rate to ensure stable operation. Each calibration curve in Figure S4 in the Supporting Information was fit using a linear regression model (least-squares approach), $y = Sx + c$, where S is the slope of the calibration (i.e., sensitivity), and c is the y-intercept. When $c < 0$, the fit was forced through zero. The fit parameters are tabulated in Table S1 in the Supporting Information. The mass LODs were obtained by computing the standard error of the regression, $\sigma_y = (\sum (\hat{y}_i - y_i)^2/(n-2))^{1/2}$, where n represents the number of data points (listed in Table S1 in Supporting Information), while $\hat{y}$ represents the predicted response. The detection limits were computed using LOD = $3\sigma_y/S$.[49,50]

The mass LODs of TREAS for TiO_2 were determined as 155 (±5) ng and 250 (±30) ng using RS and SES, respectively. The mass LODs for α-quartz were 420 (±30) ng and 900 (±100) ng using RS and SES, respectively. These mass LODs are equivalent to LODs in terms of air concentration of 42 $\mu g/m^3$ (using RS) and 90 $\mu g/m^3$ (using SES) for α-quartz and 15.5 $\mu g/m^3$ (using RS) and 25 $\mu g/m^3$ (using SES) for TiO_2 (at a flow rate of 0.5 L min^{-1} and 20 min sample collection time).

Comparing the mass LODs of TREAS for α-quartz in this study with those reported in the literature may be challenging, as variations in sample configuration, signal integration times, and spectrometer settings complicate meaningful comparisons. The LOD of α-quartz via Raman spectroscopy (0.42 μg) appears to be marginally higher than the method LODs reported by Stacey et al. using benchtop Raman instruments (0.26 μg).[23,24] However, there are significant differences in signal integration time (3 s in this study versus 7 s by Stacey et al.[23,24]) and the instrumentation employed (portable CCD spectrometers in this study versus a research-grade benchtop instrument used by Stacey et al.[23,24]). The detection limit of TREAS using Raman for α-quartz appears to be comparable to that reported by our research group using a portable Raman spectrometer. In our previous study,[27] we reported LOD of 0.49 μg for α-quartz when employing a probe-based Raman system with a 5 s signal acquisition time. Variations in LOD across different studies may not be statistically significant, given differences in spot size, signal acquisition time, measurement methodologies, and the laser and spectrometer specifications used in these investigations. The detection limit of Si (as SiO_2) using SES of 900 ng corresponds to a detection limit of elemental Si (as atomic Si) of 420 ng. In our previous study,[16] we reported a detection limit for elemental Si of 0.8 ng, utilizing a comparable pulsed spark emission spectroscopy method, which is approximately 3 orders of magnitude lower, albeit with a markedly different and more efficient aerosol microconcentration technique.

https://doi.org/10.1021/acs.analchem.5c08252
Anal. Chem. 2026, 98, 11923−11934

Table 1. Analyte Mass (m_p) in Workplace Aerosols Estimated using RS and SES Measurements in TREAS[a]

source material	analyte	RS		SES	
		mass, m_p (ng)	air conc. ($\mu g/m^3$)	mass, m_p (ng)	air conc. ($\mu g/m^3$)
engineered stone A	TiO_2	700 (±30)	70 (±3)	320 (±60)	32(±6)
	α-quartz	N.D.	-	1700 (±300)	170(±30)
engineered stone B	TiO_2	N.D.	-	N.D.	-
	α-quartz	<LOD	<LOD	1200 (±200)	120(±20)
FSD	TiO_2	N.D.	-	N.D.	-
	α-quartz	1300 (±200)	130 (±20)	1500 (±200)	150(±20)

[a]The air concentration of analyte ($m_p t_c^{-1} Q_c^{-1}$) was calculated assuming a collection time, t_c, of 20 min. The collection flow rate, Q_c, was 0.5 L min^{-1}. For reference, the Permissible Exposure Limits (PELs) of an 8 h time-weighted average set by the Occupational Safety and Health Administration (OSHA) for TiO_2 and α-quartz are 15 mg $m^{-3}$and 50 μg m^{-3}, respectively.[53]

The detection limit of TREAS of 250 ng (as TiO_2 when using SES) corresponds to an elemental Ti detection limit of 150 ng (as atomic Ti), which is approximately 2 orders of magnitude greater than the value reported in our previous study (1.1 ng).[18] As previously noted, this disparity is likely attributable to the superior aerosol collection technique used previously.

The SES signal for TiO_2 and α-quartz saturated above mass loadings of 550 ng and 1600 ng, respectively (as shown in Figure S4 in the Supporting Information). However, a combination of both spectroscopies enhanced the dynamic measurement range for these aerosols in TREAS.

It is noteworthy that the detection limits of analytes in TREAS for air concentrations are substantially higher than those reported in our prior studies using comparable methodologies. This discrepancy is primarily attributable to the low aerosol sample flow rate and the reduced sample collection time employed. Longer collection periods can facilitate lower detection limits in terms of air concentration; for instance, increasing the sampling duration from 20 to 200 min could proportionally decrease the limits of detection by *a* factor of 10.

Quantification of Silica and Titanium Dioxide in Workplace Aerosols

The analytical performance of TREAS was assessed using test aerosols that were generated from or collected during workplace activities and contained an occupationally relevant particulate matrix and composition. Three aerosols containing quartz and trace amounts of TiO_2 were employed: engineered stone A, engineered stone B, and FSD. The Raman and emission spectra for each aerosol are shown in Figure 2. Engineered stones primarily consist of crystalline silica, with titanium dioxide frequently used as a pigment.

Figure 2a,b show the Raman and the emission spectra, respectively, of engineered stone A. Raman spectra exhibited vibrational modes at 449 cm^{-1} and 610 cm^{-1} (in Figure 2a, shown after background subtraction), commonly associated with rutile TiO_2,[51] whereas emission spectra of engineered stone A showed the presence of elemental silicon, titanium, and copper (Figure 2b). The TiO_2 RS peak at 449 cm^{-1} partially overlaps with the α-quartz peak at 465 cm^{-1}. In TREAS, the Raman measurement sensitivity for TiO_2 is approximately 23 times greater than that for α-quartz (based on the ratio of the corresponding calibration slopes); thus, the α-quartz peak at 465 cm^{-1} is obscured by the much stronger TiO_2 peak at 449 cm^{-1}. Therefore, α-quartz in engineered stone A was quantified using the SES calibration (in Figure S4 in the Supporting Information), as shown in Table 1. Based on RS, the quantified TiO_2 mass was 700 (±30) ng while the SES measurements yielded a TiO_2 mass of 320 (±60) ng. The observed discrepancy between the mass measured by RS and SES is attributed to saturation of the SES calibration curve at concentrations exceeding 550 ng, and the greater spread of measured intensities within the 95% confidence interval in Figure S4 in the Supporting Information.

Figure 2c–f show the Raman and emission spectra of engineered stone B and FSD. Engineered stone B and FSD contained elemental silicon, as indicated by the SES spectra (Figure 2d,f). The presence of α-quartz was confirmed through deconvolution of the RS spectra shown in Figure 2c,e. The deconvoluted SiO_2 peak was obtained by assuming the presence of three known Raman features within the 356–550 cm^{-1} range: two background peaks at 449 and 495 cm^{-1}, and the α-quartz peak at 465 cm^{-1}, with no additional interfering peaks in this spectral region. The two background peaks were modeled with fixed area and full width half-maximum (FWHM), as listed in Table S2 in the Supporting Information. According to Table S2 in the Supporting Information, the FWHM of the α-quartz RS peak across all calibration samples was independent of mass loading, and ranged from 27 to 35 cm^{-1}, with an average value of 30 (±3) cm^{-1}. This FWHM value was therefore held constant during the deconvolution in Figure 2c,e), leaving the peak area at 465 cm^{-1} as the only free fitting parameter.

The Raman intensity measured from the deconvoluted α-quartz peak in engineered stone B (Figure 2c) was outside the intensity range of the calibration curve of Figure S4 in the Supporting Information, requiring extrapolation toward lower mass loadings. However, α-quartz calibration samples with mass loadings <770 ng did not yield any detectable Raman intensity; thus, α-quartz present in engineered stone B could not be quantified using RS. In contrast, SES measurements yielded a SiO_2 mass of 1200 (±200) ng, sufficient, in principle, to be detected by RS. The presence of amorphous silica as recycled glass in engineered stones,[34,52] which can be detected as elemental silica in emission spectroscopy, but does not contribute to the 465 cm^{-1} Raman vibration mode could explain the observed discrepancy. This discrepancy may also stem from the assumptions required for the deconvolution (e.g., fixed background peak parameters) or from potential interference by secondary compounds not accounted for in the deconvolution model. Such discrepancies highlight the need for onsite orthogonal analytical techniques to reliably detect and quantify hazardous aerosols. On the other hand, RS and SES were in good agreement for the FSD sample, yielding 1300 (±200) ng of α-quartz and 1500 (±200) ng of SiO_2, respectively (Figure 2e,f).

https://doi.org/10.1021/acs.analchem.5c08252
Anal. Chem. 2026, 98, 11923–11934

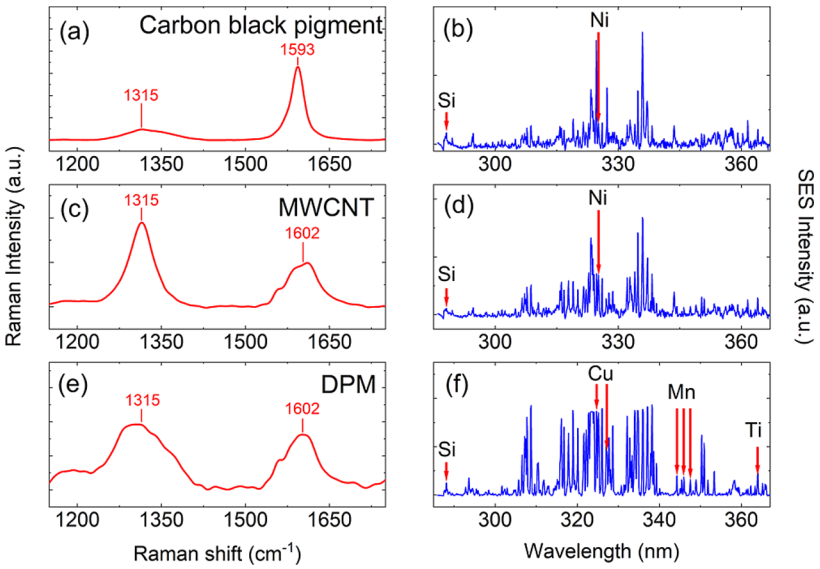

Figure 3. Raman (left) and emission (right) spectra of carbonaceous aerosols measured using TREAS—(a,b): carbon black; (c,d): CNT; and (e,f): DPM.

In Figure 2c the Raman spectrum shows a peak at 615 cm^{-1}, which, after deconvolution resolved into three peaks at 585, 617, and 645 cm^{-1}. None of these corresponds to the characteristic TiO_2 Raman peak. Similarly, in Figure 2e, an observed peak at 610 cm^{-1} was deconvoluted into four components at 582, 600, 625, and 649 cm^{-1} - again, none corresponding to the expected TiO_2 vibrational mode. Therefore, RS was unable to quantify TiO_2 in either engineered stone B or FSD.

SES results likewise indicated the absence of elemental titanium in both materials (Figure 2d,f). This finding is consistent for engineered stone B, but not for the FSD sample, as elemental Ti was detected in the FSD sample by ED-XRF analysis (Table S3 in the Supporting Information for ED-XRF elemental composition). FSD also contained other minerals such as Fe, as indicated by SES and verified by ED-XRF analysis; whereas any TiO_2 present in FSD was likely at trace levels below the detection limits of RS (<155 ng) and SES (<250 ng).

Specificity of Measurements for Other Analytes

The specificity of the measurement in other occupationally relevant aerosol matrices was probed by directly depositing the analyte-containing sample onto the collection electrode of TREAS. RS and SES spectra of carbon black are shown in Figure 3a,b, of MWCNTs in Figure 3c,d, and of DPM in Figure 3e,f, as measured using the TREAS. All carbon-based materials, irrespective of whether they are amorphous or crystalline, exhibit characteristic first-order Raman peaks at approximately 1310 cm^{-1} and 1600 cm^{-1} (Figure 3a,c and e; commonly referred to as the D and G bands, respectively).[54,55] The G band is attributed to the stretching of a bond connecting two sp^2 sites arranged in either olefinic chains or aromatic rings, while the D band arises from breathing vibrations of 6-fold aromatic rings.[30] The presence of elemental silicon in carbon black (Figure 3b) is likely due to tetraethyl orthosilicate used in its production,[56] while the Ni signal may be due to metal impurities in the feedstock.[57] Elemental Ni in Figure 3d was likely from the substrate used in CNT production.[58] Elemental Cu, Mn, and Ti in DPM (Figure 3f) were detected using SES,[17] while the characteristic emission line for carbon lies beyond the wavelength range of the optical spectrometer used in TREAS. Instead, the carbon content in these aerosols can be quantified using either the D or G Raman bands, as shown earlier.[30] Selectivity to a specific type of carbonaceous component (e.g., polymorph) may not be possible based on just the Raman spectra, as all polymorphs exhibit D and G bands. The elemental markers from SES, specific to the particulate matrix, could possibly be used to narrow down chemical specificity.

Stainless steel welding fumes may contain a range of metal oxides and spinel-type oxides, including Fe_3O_4, Fe_2O_3, Mn_3O_4, Mn_2O_3, Cr_2O_3, and $FeCr_2O_4$, among others.[59−62] Among these species, hexavalent chromium [Cr(VI)] compounds are of particular concern, due to their acute health risks, and are therefore often the primary analytes of interest in particulate matter speciation.[63,64]

Figure 4 shows the Raman spectra of chromium species representing different valence states, along with the Raman spectrum obtained from the aerosolized welding fume reference material (referred to here as welding aerosol). Cr_2O_3 (Figure 4a) and $Cr_2O_4^{2-}$ (Figure 4b) contain chromium in the trivalent oxidation state [Cr(III)], whereas CrO_4^{-2} (Figure 4c) contains chromium in its hexavalent state [Cr(VI)]. The primary characteristic Raman peak of Cr_2O_3 appears at approximately 554 cm^{-1}, corresponding to the symmetric Cr−O stretching in octahedral coordination (A_{1g} vibrational mode).[65] A weaker band is observed at 617 cm^{-1}, attributed to the Cr−O stretching mode.[66] In Figure 4b, the main characteristic peak of $Cr_2O_4^{2-}$ associated with the symmetric Cr−O stretching of octahedra CrO_6, is shown at approximately 694 cm^{-1}, with a shoulder peak at approximately 650 cm^{-1}.[67,68] Figure 4c shows the strongest Raman peak of CrO_4^{2-} at 839 cm^{-1}, which corresponds to the symmetric Cr−O stretching (A_{1g} vibrational mode).[69] The characteristic Raman bands of Cr_2O_3 and $Cr_2O_4^{-2}$, both containing trivalent chromium, and that of CrO_4^{-2}, containing hexavalent chromium, are distinct and can therefore be used to speciate the two oxidation states.

The Raman spectrum of the aerosolized stainless steel welding fume reference material is shown in Figure 4d. The

https://doi.org/10.1021/acs.analchem.5c08252
Anal. Chem. 2026, 98, 11923−11934

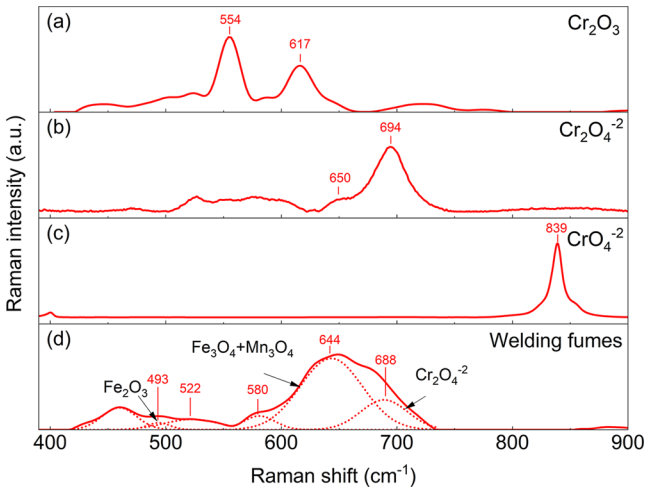

Figure 4. Raman spectra of chromium-containing aerosols measured using TREAS: (a) Cr_2O_3 (Cr(III)), (b) $Cr_2O_4^{2-}$ (Cr(III)), (c) CrO_4^{2-} (Cr(VI)), and (d) stainless steel welding fumes. Raman spectra of $Cr_2O_4^{2-}$($FeCr_2O_4$) in (b) and CrO_4^{2-}($Pb(CrO_4)$) in (c) were obtained from the literature.[38]

main characteristic peak of CrO_4^{2-} does not appear, indicating the absence of detectable hexavalent chromium in the welding fume sample. However, trace amounts of Cr (VI) could still be present below the detection limits of TREAS. A peak appearing at approximately 688 cm^{-1}, obtained after deconvolution of the broader feature near 649 cm^{-1}, may correspond to the symmetric Cr−O stretching of octahedra CrO_6 in $Cr_2O_4^{2-}$ (Figure 4b). The characteristic peak of Cr_2O_3 is also not shown in Figure 4d.

Figure 5 shows the SES spectra of chromium-containing reference materials and the welding fume sample. Figure 5a,b

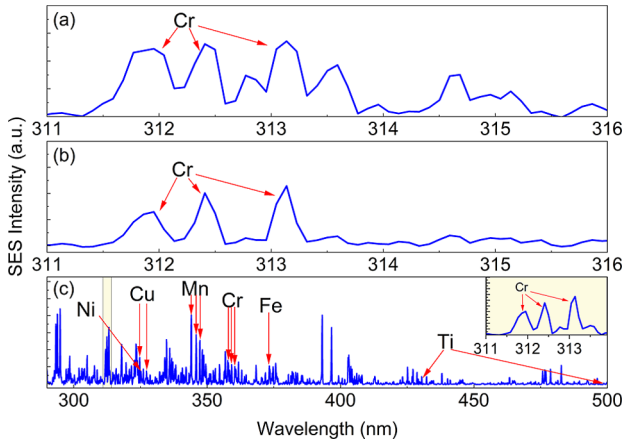

Figure 5. SES spectra of chromium-containing aerosols measured using TREAS: (a) Cr_2O_3; (b) aqueous Cr (VI) solution; (c) stainless steel welding fumes. The inset in (c) shows a magnified view of the shaded region of the main spectrum, highlighting the three characteristic chromium emission peaks.

show the elemental signatures of Cr_2O_3 and aqueous hexavalent chromium solution, both exhibiting the same three characteristic Cr peaks at 312, 312.4, and 313 nm. The SES spectrum of the stainless steel welding fume (Figure 5c) also shows these three Cr peaks, confirming the presence of chromium in the aerosol sample.

The absence of the characteristic CrO_4^{2-} Raman peak and the presence of a potential $Cr_2O_4^{2-}$ band indicate that chromium in the stainless steel welding fume is predominantly in the trivalent oxidation state. The remaining deconvoluted Raman peaks in Figure 4d are likely due to interference from other welding fume matrix components such as Fe_3O_4, Fe_2O_3, and Mn_3O_4.[38] The presence of elemental Ni, Cu, Mn, Cr, and Ti detected by TREAS (Figure 5c) is consistent with previously reported stainless steel welding fume compositions[70] and with our ED-XRF analysis of the same sample (Table S3 in the Supporting Information). Overall, these results demonstrate the utility of TREAS for aerosol measurements, particularly in applications where specificity with respect to chemical speciation or oxidative state is desirable.

Near-Real-Time Automated Measurement with TREAS

Titanium dioxide aerosol was used to assess TREAS's continuous, automated measurement capability for capturing variation in transient aerosol concentration. TiO_2 powder was aerosolized using a fluidized-bed aerosol generator. The concentration of the resulting TiO_2 aerosol was varied at 1 min intervals. Figure 6 shows continuous measurements of the

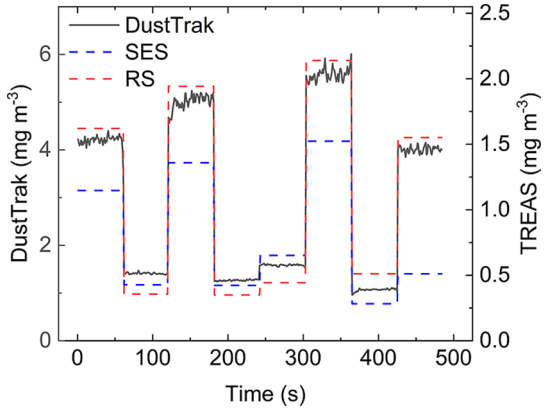

Figure 6. Short-term measurement of titanium dioxide aerosol concentration using TREAS in a transient aerosol simulating work activity. The aerosol concentration was also simultaneously monitored using the field-portable DustTrak DRX monitor. RS and SES measurements were collected at a 1 min time resolution, while the DRX monitor had a 1 s resolution.

mass concentration of the titanium dioxide aerosol monitored with a DustTrak DRX Aerosol Monitor (model 8533, TSI Inc., Shoreview, MN, USA), while consecutive 1 min samples were collected for RS and SES analysis in TREAS. This collection time was sufficient to measure above the LOD of RS and SES. In Figure 6, the solid black curve shows the real-time total aerosol mass concentration measured by the DRX aerosol monitor (left axis). The time resolution of DRX monitor was 1 s, significantly higher than that of TREAS (1 min). The dashed red and blue curves show the measured TiO_2 concentration measured by TREAS using RS and SES (right axis). The TREAS captured variation in aerosol concentration, consistent with DRX measurements, demonstrating its ability to obtain continuous, automated, near-real-time measurements. Concentration measured by TREAS using RS agrees reasonably well, given the differences in measurement techniques between the two instruments (optical counter versus spectroscopy) and the particle size ranges sampled by both instruments. Notably, the agreement between SES and TREAS measurements was

https://doi.org/10.1021/acs.analchem.5c08252
Anal. Chem. 2026, 98, 11923−11934

poor, particularly at higher concentrations. We believe this was due to particulate mass loading beyond the calibration curve's working range (loadings >550 ng, as noted previously and shown in Figure S4 in the Supporting Information), resulting in saturation of the SES spectrometer.

Measurement Uncertainty

Multiple factors impact the overall uncertainty in the quantification of analytes using TREAS. The primary sources of uncertainty include variations in sampling flow rate, aerosol size distribution, the intensity of the Raman excitation laser, HV spark characteristics, CCD spectrometer noise, and the rotational and alignment precision of the collection electrode. Since rotational accuracy is specific to TREAS and distinguishes it from other well-characterized, controllable factors, it was investigated further to assess its influence on spectroscopic measurement uncertainty. Since TREAS involves cyclic rotational movements in both clockwise and counterclockwise directions, cumulative errors in the rotational angle can alter the orientation of the planar collection electrode relative to the nozzle, excitation laser, or anode, consequently influencing aerosol mass collection or spectroscopic signal measurement. The collection electrode was subjected to repeated rotations of 100, 500, and 1000 cycles to evaluate cumulative orientation changes, which were determined to be negligible. Furthermore, the electrode was intentionally misaligned by 5°, and the resulting variation in the Raman signal was measured relative to the baseline orientation of 0°, which resulted in an uncertainty of 10−15% in the measured RS signal.

The uncertainty associated with the Raman calibration curve derived from the standard error of the regression was estimated at 4−5%. When these factors are considered collectively, the resulting combined uncertainty ranges from 11% to 16% for mass measurement via RS. Similarly, the 5° misalignment led to an uncertainty of 7% in the measured SES signal. This uncertainty, combined with the uncertainty in the slope of RS calibration curves (5−13%), resulted in a 9−15% uncertainty in mass measurement via SES. The uncertainty in the aerosol sample flow rate was estimated at 5−10%. Using propagation of errors, the overall uncertainty in the measurement of aerosol concentration ranged from 12% to 19% when using RS, and from 10% to 18% when using SES in TREAS. These are approximate estimates and do not account for errors in particle mass collection by TREAS due to variations in the aerosol size distribution (attributable to the strong size-dependent collection efficiency of the nozzle employed) and other sources of uncertainty.

Limitations of TREAS Measurements

While the TREAS instrument demonstrates significant potential for near-real-time aerosol monitoring, the current prototype is subject to two key limitations that affect analytical performance. First, the aerosol collection system, which relies on a single converging nozzle, operates at a relatively low sampling flow rate (0.5 lpm) and induces a higher pressure drop. The impaction process also results in a somewhat ill-defined sample spot on the collection electrode, which can compromise the overlap with the Raman laser focal point and the spark discharge. As noted earlier, impaction collection efficiency is also particle-size dependent. Particle bounce, which is pronounced at larger particle sizes, further introduces additional artifacts in the collection efficiency estimation. These factors collectively increase uncertainty and limit the mass accumulation rate, thereby reducing the instrument's analytical sensitivity and time resolution. To address these limitations, high-throughput spot-sampling methods using turbulent mixing condensational growth have been developed in our laboratory[46,47] and have been demonstrated to improve collection efficiency and spot morphology, regardless of the size distribution of the sampled aerosol. Integration of such high-flow interfaces into the next generation of TREAS platform is currently underway to enhance sensitivity and reduce sampling intervals.

Second, fluorescence interference remains a known challenge for Raman spectroscopy, particularly when analyzing environmental samples containing organic or biogenic materials. This background signal can obscure weak Raman scattering features, complicating spectral analysis. Potential strategies to mitigate fluorescence include using shorter signal integration times or implementing pulsed laser excitation schemes, which can temporally discriminate between instantaneous Raman scattering and longer-lived fluorescence. Future iterations of TREAS will explore these optical refinements to broaden the instrument's applicability to complex organic-rich aerosols.

TREAS measurements of workplace aerosols may be influenced by interference from ubiquitous atmospheric aerosol components, such as secondary organic aerosols, nitrates, sulfates, and polycyclic aromatic hydrocarbons (PAHs). Table S4 in the Supporting Information provides the characteristic Raman shift values for major atmospheric aerosol constituents. Raman-active vibrational modes of common organic functional groups (e.g., C−C, C−H, C═O, and O−H) and inorganic species (e.g., NO_3^-, NH_4^+, SO_4^{2-}, CO_3^{2-}) typically produce peaks at wavenumbers above 1000 cm^{-1}, which are unlikely to overlap with the α-quartz, TiO_2, and other inorganic peaks of interest below 1000 cm^{-1}. Conversely, sulfates exhibit a Raman band near 450 cm^{-1}, which partially overlaps with the α-quartz peak at 465 cm^{-1}. When such overlap occurs, spectral deconvolution using peak-fitting can be employed to separate the peaks. Given that atmospheric aerosol concentrations are generally lower than those encountered in occupational environments by an order of magnitude, spectral interference from background atmospheric components is expected to be minimal in most workplaces.

CONCLUSIONS

We have presented the design, development, and performance evaluation of the Tandem Raman and Elemental Aerosol Spectrometer (TREAS), a compact, field-portable instrument developed for the near-real-time characterization of occupational aerosols. By utilizing an automated cyclical "collection-analysis-ablation" scheme, the instrument successfully integrates orthogonal spectroscopic techniques, Raman spectroscopy (RS) and Spark Emission Spectroscopy (SES), to provide concurrent molecular and elemental speciation. The instrument demonstrated high sensitivity for hazardous workplace aerosols. The mass limits of detection (LODs) for α-quartz were 420 ng (RS) and 900 ng (SES), while LODs for titanium dioxide were 155 ng (RS) and 250 ng (SES). These detection limits are orders of magnitude lower than those of standard off-line X-ray diffraction methods.

Validation tests using complex matrices, including engineered stone dust and fracking sand, confirmed the instrument's ability to identify and measure analytes in mixed

https://doi.org/10.1021/acs.analchem.5c08252
Anal. Chem. 2026, 98, 11923−11934

aerosols. The tandem approach was especially useful for determining oxidation states, successfully distinguishing between Cr (III) and Cr (VI) in welding fumes, a distinction vital for risk assessment. Overall, the superior sensitivity, chemical specificity, and time resolution of TREAS can provide a reliable solution for on-site exposure monitoring and atmospheric aerosol measurement.

■ ASSOCIATED CONTENT

Supporting Information

The Supporting Information is available free of charge at https://pubs.acs.org/doi/10.1021/acs.analchem.5c08252.

TREAS prototype and layout. Nozzle collection efficiency, schematic for instrument calibration, calibration curves and fit parameters for TiO_2 and SiO_2, peak properties after spectral deconvolution, elemental composition of test materials and peak Raman scattering frequencies for organic and inorganic species in atmospheric aerosol (PDF)

■ AUTHOR INFORMATION

Corresponding Author

Pramod Kulkarni − *Centers for Disease Control and Prevention (CDC), National Institute for Occupational Safety and Health (NIOSH), Cincinnati 45226 Ohio, United States; Department of Environmental and Public Health Sciences, University of Cincinnati, College of Medicine, Cincinnati 45267 Ohio, United States;* orcid.org/0000-0001-7692-4662; Phone: Phone: + 1 (513) 841-4300; Email: PSKulkarni@cdc.gov

Authors

Nicholas Pugh − *Centers for Disease Control and Prevention (CDC), National Institute for Occupational Safety and Health (NIOSH), Cincinnati 45226 Ohio, United States; Department of Mechanical Engineering, South Dakota School of Mines & Technology, Rapid City 57701 South Dakota, United States*

Orthodoxia Zervaki − *Centers for Disease Control and Prevention (CDC), National Institute for Occupational Safety and Health (NIOSH), Cincinnati 45226 Ohio, United States*

Kabir Rishi − *Centers for Disease Control and Prevention (CDC), National Institute for Occupational Safety and Health (NIOSH), Cincinnati 45226 Ohio, United States;* orcid.org/0000-0002-3159-031X

Surendra Devarakonda − *Centers for Disease Control and Prevention (CDC), National Institute for Occupational Safety and Health (NIOSH), Cincinnati 45226 Ohio, United States*

Complete contact information is available at: https://pubs.acs.org/10.1021/acs.analchem.5c08252

Notes

The authors declare no competing financial interest.

Disclaimer: The findings and conclusions in this report are those of the authors and do not necessarily represent the official position of the National Institute for Occupational Safety and Health, Centers for Disease Control and Prevention. Mention of any company or product does not constitute endorsement by the National Institute for Occupational Safety and Health, Centers for Disease Control and Prevention. DisclaimerThe findings and conclusions in this report are those of the author(s) and do not necessarily represent the official position of the National Institute for Occupational Safety and Health (NIOSH), Centers for Disease Control and Prevention (CDC). The mention of any company or product does not constitute an endorsement by NIOSH.

■ ACKNOWLEDGMENTS

This research work was supported by a NIOSH intramural NORA grant 9390G1Y. The authors would like to thank Dr. Bon-Ki Ku for assisting with the experiments.

■ REFERENCES

(1) Pope III, C. A.; Burnett, R. T.; Thun, M. J.; Calle, E. E.; Krewski, D.; Thurston, G. D. Lung Cancer, Cardiopulmonary Mortality, and Long-Term Exposure to Fine Particulate Air Pollution. *JAMA* **2002**, *287* (9), 1132−1141.

(2) Misra, S.; Sussell, A. L.; Wilson, S. E.; Poplin, G. S. Occupational Exposure to Respirable Crystalline Silica among US Metal and Nonmetal Miners, 2000−2019. *Am. J. Ind. Med.* **2023**, *66* (3), 199−212.

(3) NIOSH. Silica, Crystalline, by XRD: Method 7500. *NIOSH Man. Anal. Methods* **2003**, No. 4, 3233−3250.

(4) MSHA. Infrared Determination of Quartz in Respirable Coal Mine Dust: Method P-7. In *Mine Saf. Heal. Div. Pittsburgh Saf. Heal. Technol.*; Cent, 2013; pp 1−18.

(5) Hofman, J.; Lazarov, B.; Stroobants, C.; Elst, E.; Smets, I.; Van Poppel, M. Portable Sensors for Dynamic Exposure Assessments in Urban Environments: State of the Science. *Sensors* **2024**, *24* (17), 5653.

(6) Liu, H.; Wang, Z.; Zhou, G. Wearable Sensors for Monitoring Workplace Chemical Exposures in Occupational Health Management. *Anal. Methods* **2025**, *17* (39), 7863−7889.

(7) Butler, O. T.; Cairns, W. R. L.; Cook, J. M.; Davidson, C. M. Atomic Spectrometry Update − a Review of Advances in Environmental Analysis. *J. Anal. At. Spectrom.* **2017**, *32* (1), 11−57.

(8) Montaño, M. D.; Olesik, J. W.; Barber, A. G.; Challis, K.; Ranville, J. F. Single Particle ICP-MS: Advances toward Routine Analysis of Nanomaterials. *Anal. Bioanal. Chem.* **2016**, *408* (19), 5053−5074.

(9) Canagaratna, M. R.; Jayne, J. T.; Jimenez, J. L.; Allan, J. D.; Alfarra, M. R.; Zhang, Q.; Onasch, T. B.; Drewnick, F.; Coe, H.; Middlebrook, A.; Delia, A.; Williams, L. R.; Trimborn, A. M.; Northway, M. J.; DeCarlo, P. F.; Kolb, C. E.; Davidovits, P.; Worsnop, D. R. Chemical and Microphysical Characterization of Ambient Aerosols with the Aerodyne Aerosol Mass Spectrometer. *Mass Spectrom. Rev.* **2007**, *26* (2), 185−222.

(10) Zelenyuk, A.; Imre, D. Beyond Single Particle Mass Spectrometry: Multidimensional Characterisation of Individual Aerosol Particles. *Int. Rev. Phys. Chem.* **2009**, *28* (2), 309−358.

(11) Tremper, A. H.; Font, A.; Priestman, M.; Hamad, S. H.; Chung, T.-C.; Pribadi, A.; Brown, R. J. C.; Goddard, S. L.; Grassineau, N.; Petterson, K.; Kelly, F. J.; Green, D. C. Field and Laboratory Evaluation of a High Time Resolution X-Ray Fluorescence Instrument for Determining the Elemental Composition of Ambient Aerosols. *Atmos. Meas. Technol.* **2018**, *11* (6), 3541−3557.

(12) Dudani, N.; Takahama, S. Design and Fabrication of an Electrostatic Precipitator for Infrared Spectroscopy. *Atmos. Meas. Technol.* **2022**, *15* (16), 4693−4707.

(13) Diwakar, P.; Kulkarni, P.; Birch, M. E. New Approach for Near-Real-Time Measurement of Elemental Composition of Aerosol Using Laser-Induced Breakdown Spectroscopy. *Aerosol Sci. Technol.* **2012**, *46* (3), 316−332.

(14) Kulkarni, P.; Efthimion, P. Electrode-Assisted Microwave-Induced Plasma Spectroscopy. U.S.9091597 B2, 2015. https://patents.google.com/patent/US9091597B2/en.
(15) Zheng, L.; Kulkarni, P. Rapid Elemental Analysis of Aerosols Using Atmospheric Glow Discharge Optical Emission Spectroscopy. *Anal. Chem.* **2017**, *89* (12), 6551−6558.
(16) Diwakar, P. K.; Kulkarni, P. Measurement of Elemental Concentration of Aerosols Using Spark Emission Spectroscopy. *J. Anal. At. Spectrom.* **2012**, *27* (7), 1101−1109.
(17) Zheng, L.; Kulkarni, P.; Birch, M. E.; Deye, G.; Dionysiou, D. D. Near Real-Time Measurement of Carbonaceous Aerosol Using Microplasma Spectroscopy: Application to Measurement of Carbon Nanomaterials. *Aerosol Sci. Technol.* **2016**, *50* (11), 1155−1166.
(18) Zheng, L.; Kulkarni, P.; Dionysiou, D. D. Calibration Approaches for the Measurement of Aerosol Multielemental Concentration Using Spark Emission Spectroscopy. *J. Anal. At. Spectrom.* **2018**, *33* (3), 404−412.
(19) Kulkarni, P.; Zheng, L.; Deye, G.; Birch, M. E. Abstract T106N2dd: Aerosol Multielement Spectrometer for Near Real-Time Measurement of Aerosol Elemental Concentration. In *23rd European Aerosol Conference*; Zurich, Switzerland, 2017. DOI: 10.22541/essoar.176192379.92238731/v1.
(20) Li, H.; Mazzei, L.; Wallis, C. D.; Davari, S. A.; Wexler, A. S. The Performance of an Inexpensive Spark-Induced Breakdown Spectroscopy Instrument for near Real-Time Analysis of Toxic Metal Particles. *Atmos. Environ.* **2021**, *264*, 118666.
(21) Li, J.; Huang, J.; Zheng, L.; Naz, S.; Liu, X. Fast Analysis of Metal Components in Coal Dust Using Spark Emission Spectroscopy. *J. Anal. At. Spectrom.* **2024**, *39* (12), 3171−3179.
(22) Olson, N. E.; Xiao, Y.; Lei, Z.; Ault, A. P. Simultaneous Optical Photothermal Infrared (O-PTIR) and Raman Spectroscopy of Submicrometer Atmospheric Particles. *Anal. Chem.* **2020**, *92* (14), 9932−9939.
(23) Stacey, P.; Mader, K. T.; Sammon, C. Feasibility of the Quantification of Respirable Crystalline Silica by Mass on Aerosol Sampling Filters Using Raman Microscopy. *J. Raman Spectrosc.* **2017**, *48* (5), 720−725.
(24) Stacey, P.; Clegg, F.; Morton, J.; Sammon, C. An Indirect Raman Spectroscopy Method for the Quantitative Measurement of Respirable Crystalline Silica Collected on Filters inside Respiratory Equipment. *Anal. Methods* **2020**, *12* (21), 2757−2771.
(25) Doughty, D. C.; Hill, S. C. Automated Aerosol Raman Spectrometer for Semi-Continuous Sampling of Atmospheric Aerosol. *J. Quant. Spectrosc. Radiat. Transfer* **2017**, *188*, 103−117.
(26) Grafen, M.; Schweiger, G.; Esen, C.; Ostendorf, A. Time-Resolved Measurement of Elemental Carbon in Urban Environment: Comparison of Raman Backscattering and Aethalometer Results. *J. Aerosol Sci.* **2018**, *117*, 34−43.
(27) Zheng, L.; Kulkarni, P.; Birch, M. E.; Ashley, K.; Wei, S. Analysis of Crystalline Silica Aerosol Using Portable Raman Spectrometry: Feasibility of Near Real-Time Measurement. *Anal. Chem.* **2018**, *90* (10), 6229−6239.
(28) Wei, S.; Johnson, B.; Breitenstein, M.; Zheng, L.; Snawder, J.; Kulkarni, P. Aerosol Analysis Using Handheld Raman Spectrometer: On-Site Quantification of Trace Crystalline Silica in Workplace Atmospheres. *Ann. Work Expo. Heal.* **2022**, *66* (5), 656−670.
(29) Zervaki, O.; Stump, B.; Keady, P.; Dionysiou, D. D.; Kulkarni, P. NanoSpot TM Collector for Aerosol Sample Collection for Direct Microscopy and Spectroscopy Analysis. *Aerosol Sci. Technol.* **2023**, *57* (4), 342−354.
(30) Zheng, L.; Kulkarni, P. Real-Time Measurement of Airborne Carbon Nanotubes in Workplace Atmospheres. *Anal. Chem.* **2019**, *91* (20), 12713−12723.
(31) Huffman, J. A.; Perring, A. E.; Savage, N. J.; Clot, B.; Crouzy, B.; Tummon, F.; Shoshanim, O.; Damit, B.; Schneider, J.; Sivaprakasam, V.; Zawadowicz, M. A.; Crawford, I.; Gallagher, M.; Topping, D.; Doughty, D. C.; Hill, S. C.; Pan, Y. Real-Time Sensing of Bioaerosols: Review and Current Perspectives. *Aerosol Sci. Technol.* **2020**, *54* (5), 465−495.
(32) Zervaki, O.; Dionysiou, D. D.; Kulkarni, P. Characterization of a Multi-Stage Focusing Nozzle for Collection of Spot Samples for Aerosol Chemical Analysis. *J. Aerosol Sci.* **2023**, *174* (4), 106235.
(33) Ramkissoon, C.; Gaskin, S.; Song, Y.; Pisaniello, D.; Zosky, G. R. From Engineered Stone Slab to Silicosis: A Synthesis of Exposure Science and Medical Evidence. *Int. J. Environ. Res. Public Health* **2024**, *21* (6), 683.
(34) Rishi, K.; Ku, B. K.; Qi, C.; Thompson, D.; Wang, C.; Dozier, A.; Vogiazi, V.; Zervaki, O.; Kulkarni, P. Release of Crystalline Silica Nanoparticles during Engineered Stone Fabrication. *ACS Omega* **2024**, *9* (51), 50308−50317.
(35) Ku, B. K.; Deye, G.; Turkevich, L. A. Characterization of a Vortex Shaking Method for Aerosolizing Fibers. *Aerosol Sci. Technol.* **2013**, *47* (12), 1293−1301.
(36) Esswein, E. J.; Breitenstein, M.; Snawder, J.; Kiefer, M.; Sieber, W. K. Occupational Exposures to Respirable Crystalline Silica During Hydraulic Fracturing. *J. Occup. Environ. Hyg.* **2013**, *10* (7), 347−356.
(37) Fedan, J. S.; Hubbs, A. F.; Barger, M.; Schwegler-Berry, D.; Friend, S. A.; Leonard, S. S.; Thompson, J. A.; Jackson, M. C.; Snawder, J. E.; Dozier, A. K.; Coyle, J.; Kashon, M. L.; Park, J.-H. H.; McKinney, W.; Roberts, J. R. Biological Effects of Inhaled Hydraulic Fracturing Sand Dust. II. Particle Characterization and Pulmonary Effects 30 d Following Intratracheal Instillation. *Toxicol. Appl. Pharmacol.* **2020**, *409* (July), 115282.
(38) Lafuente, B.; Downs, R. T.; Yang, H.; Stone, N. 1. The Power of Databases: The RRUFF Project. In *Highlights in Mineralogical Crystallography*; DE GRUYTER, 2015; pp 1−30.
(39) Yan, J.; Wu, G.; Guan, N.; Li, L.; Li, Z.; Cao, X. Understanding the Effect of Surface/Bulk Defects on the Photocatalytic Activity of TiO2: Anatase versus Rutile. *Phys. Chem. Chem. Phys.* **2013**, *15* (26), 10978−10988.
(40) Zhang, Y.; Harris, C. X.; Wallenmeyer, P.; Murowchick, J.; Chen, X. Asymmetric Lattice Vibrational Characteristics of Rutile TiO 2 as Revealed by Laser Power Dependent Raman Spectroscopy. *J. Phys. Chem. C* **2013**, *117* (45), 24015−24022.
(41) Ekoi, E. J.; Gowen, A.; Dorrepaal, R.; Dowling, D. P. Characterisation of Titanium Oxide Layers Using Raman Spectroscopy and Optical Profilometry: Influence of Oxide Properties. *Results Phys.* **2019**, *12*, 1574−1585.
(42) Kramida, A.; Ralchenko, Y.; Reader, J. Atomic Spectra Database. *NIST Standard Reference Database 78*, Version 5.11, 2023. DOI: 10.18434/T4W30F.
(43) Stacey, P.; Kauffer, E.; Moulut, J. C.; Dion, C.; Beauparlant, M.; Fernandez, P.; Key-Schwartz, R.; Friede, B.; Wake, D. An International Comparison of the Crystallinity of Calibration Materials for the Analysis of Respirable α-Quartz Using X-Ray Diffraction and a Comparison with Results from the Infrared KBr Disc Method. *Ann. Occup. Hyg.* **2009**, *53* (6), 639−649.
(44) Kajiwara, T.; Ogami, A.; Yamato, H.; Oyabu, T.; Morimoto, Y.; Tanaka, I. Effect of Particle Size of Intratracheally Instilled Crystalline Silica on Pulmonary Inflammation. *J. Occup. Health* **2007**, *49* (2), 88−94.
(45) HORIBA. Titanium Dioxide Particle Size. https://www.horiba.com/int/scientific/applications/chemistry/pages/titanium-dioxide-particle-size/(accessed 01 November 2025).
(46) Zervaki, O.; Dionysiou, D. D.; Kulkarni, P. Compact, High-Flow, Water-Based, Turbulent-Mixing, Condensation Aerosol Concentrator for Collection of Spot Samples. *Aerosol Sci. Technol.* **2024**, *58* (8), 889−901.
(47) Zervaki, O.; Dionysiou, D. D.; Kulkarni, P. A High-Turbulent-Mixing Condensation Aerosol Concentrator for Direct Aerosol Collection as a Liquid Suspension. *J. Aerosol Sci.* **2024**, *182*, 106442.
(48) Kingma, K. J.; Hemley, R. J. Raman Spectroscopic Study of Microcrystalline Silica. *Am. Mineral.* **1994**, *79* (3−4), 269−273.
(49) Keith, L. H.; Crummett, W.; Deegan, J.; Libby, R. A.; Taylor, J. K.; Wentler, G. Principles of Environmental Analysis. *Anal. Chem.* **1983**, *55* (14), 2210−2218.

(50) Burkart, J. A. General Procedures for Limit of Detection Calculations in the Industrial Hygiene Laboratory. *Appl. Ind. Hyg.* **1986**, *1* (3), 153−155.
(51) Hardcastle, F. D. Raman Spectroscopy of Titania (TiO2) Nanotubular Water-Splitting Catalysts. *J. Ark. Acad. Sci.* **2011**, *65* (1), 9.
(52) Ramkissoon, C.; Pavan, C.; Petriglieri, J. R.; Fimiani, M.; Pisaniello, D.; Gaskin, S.; Turci, F. Physico-Chemical Features and Membranolytic Activity of Dust from Low or No Crystalline Silica Engineered Stone with Implications for Toxicological Assessment. *Sci. Rep.* **2025**, *15* (1), 25451.
(53) OSHA *Permissible Exposure Limits − Annotated Tables*, 2021.
(54) Wu, J.-B.; Lin, M.-L.; Cong, X.; Liu, H.-N.; Tan, P.-H. Raman Spectroscopy of Graphene-Based Materials and Its Applications in Related Devices. *Chem. Soc. Rev.* **2018**, *47* (5), 1822−1873.
(55) Dovbeshko, G.; Fesenko, O.; Dementjev, A.; Karpicz, R.; Fedorov, V.; Posudievsky, O. Y. Coherent Anti-Stokes Raman Scattering Enhancement of Thymine Adsorbed on Graphene Oxide. *Nanoscale Res. Lett.* **2014**, *9* (1), 263.
(56) Krejei, J. C. Carbon Black Process. U.S.2632713 A, 1953. https://patents.google.com/patent/US2632713A/en#patentCitations.
(57) Wolter, M.; Heymer, G. Process for the Removal of Metals from Carbon Black. U.S.4320108, 1982.
(58) Ge, C.; Li, W.; Li, Y.; Li, B.; Du, J.; Qiu, Y.; Liu, Y.; Gao, Y.; Chai, Z.; Chen, C. Significance and Systematic Analysis of Metallic Impurities of Carbon Nanotubes Produced by Different Manufacturers. *J. Nanosci. Nanotechnol.* **2011**, *11* (3), 2389−2397.
(59) Antonini, J. M. Health Effects of Welding. *Crit. Rev. Toxicol.* **2003**, *33* (1), 61−103.
(60) Zimmer, A. T.; Biswas, P. Characterization of the Aerosols Resulting from Arc Welding Processes. *J. Aerosol Sci.* **2001**, *32* (8), 993−1008.
(61) Hewitt, P. J.; Gray, C. N. Some Difficulties in the Assessment of Electric Arc Welding Fume. *Am. Ind. Hyg. Assoc. J.* **1983**, *44* (10), 727−732.
(62) Owen, B..; Material Safety Data Sheet SSWF-1: Derbyshire, UK, 2019. https://solutions.hse.gov.uk/media/232082/material/safety/data/sheet/sswf-1/-/v2.pdf.
(63) Sandana Mala, J. G.; Sujatha, D.; Rose, C. Inducible Chromate Reductase Exhibiting Extracellular Activity in Bacillus Methylotrophicus for Chromium Bioremediation. *Microbiol. Res.* **2015**, *170*, 235−241.
(64) Gu, Y.; Xu, W.; Liu, Y.; Zeng, G.; Huang, J.; Tan, X.; Jian, H.; Hu, X.; Li, F.; Wang, D. Mechanism of Cr(VI) Reduction by Aspergillus Niger: Enzymatic Characteristic, Oxidative Stress Response, and Reduction Product. *Environ. Sci. Pollut. Res.* **2015**, *22* (8), 6271−6279.
(65) Larbi, T.; Ouni, B.; Gantassi, A.; Doll, K.; Amlouk, M.; Manoubi, T. Structural, Optical and Vibrational Properties of Cr2O3 with Ferromagnetic and Antiferromagnetic Order: A Combined Experimental and Density Functional Theory Study. *J. Magn. Magn. Mater.* **2017**, *444*, 16−22.
(66) Bhardwaj, P.; Singh, J.; Kumar, R.; Kumar, D.; Verma, V.; Kumar, R. Oxygen Defects Induced Tailored Optical and Magnetic Properties of FexCr2−xO3 ($0 \leq x \leq 0.1$) Nanoparticles. *Appl. Phys. A: Mater. Sci. Process.* **2022**, *128* (2), 135.
(67) Joshi, A. C.; Rufus, A. L.; Suresh, S.; Chandramohan, P.; Rangarajan, S.; Velmurugan, S. Characterization of the Oxide Formed in the Presence of Poly Acrylic Acid over the Steam Generator Structural Materials of Nuclear Power Plants. *J. Nucl. Mater.* **2013**, *437* (1−3), 139−148.
(68) Zhang, Z. W.; Gan, F. X. Analysis of the Chromite Inclusions Found in Nephrite Minerals Obtained from Different Deposits Using SEM-EDS and LRS. *J. Raman Spectrosc.* **2011**, *42* (9), 1808−1811.
(69) Frost, R. L. Raman Microscopy of Selected Chromate Minerals. *J. Raman Spectrosc.* **2004**, *35* (2), 153−158.
(70) Butler, O.; Grosser, M. *Certification Report Reference Material HSL SSWF-01 Elements in Stainless Steel Welding Fume*; AS/2012/12; Health and Safety Laboratory: Buxton, United Kingdom, 2013.

https://doi.org/10.1021/acs.analchem.5c08252
Anal. Chem. 2026, 98, 11923−11934